Research Square

Preprints are preliminary reports that have not undergone peer review.
They should not be considered conclusive, used to inform clinical practice,
or referenced by the media as validated information.

Machine-Learning-Guided Defect-Acid Network Engineering in Zn-Modified Y Zeolites for Selective Fischer-Tropsch Wax Hydrocracking

Lu Gong

gonglu@cup.edu.cn

China University of Petroleum (Beijing)

Wenbin Huang

China University of Petroleum (Beijing)

Fan Shao

China University of Petroleum (Beijing)

Fengzhi Guo

China University of Petroleum (Beijing)

Tianyu Bai

China University of Petroleum (Beijing)

Minghui Zhang

China University of Petroleum (Beijing)

Wenbo Kang

China University of Petroleum (Beijing)

Jinxiao Sun

China University of Petroleum (Beijing)

Zhen Xu

China University of Petroleum (Beijing)

Shixuan Guo

China University of Petroleum (Beijing)

Han Yang

China University of Petroleum (Beijing)

Yasong Zhou

China University of Petroleum (Beijing)

Gang Wang

China University of Petroleum (Beijing)

Qiang Wei

China University of Petroleum (Beijing)

Article

Keywords: selective hydrocracking, interpretable machine learning, Zn-incorporated Y zeolites, Lewis acid site, jet-fuel

Posted Date: June 23rd, 2026

DOI: https://doi.org/10.21203/rs.3.rs-10018430/v1

License: This work is licensed under a Creative Commons Attribution 4.0 International License. Read Full License

Additional Declarations: There is **NO** Competing Interest.

Abstract

Selective hydrocracking of Fischer-Tropsch wax to jet-fuel-range hydrocarbons requires efficient C-C bond scission while suppressing secondary over-cracking. However, the factors that control this selectivity remain unclear because acidity, pore structure and metal function are closely intertwined in zeolitic catalysts. Here we combined interpretable machine learning with targeted catalyst synthesis to identify and validate the descriptors controlling hydrocracking selectivity over Y zeolites. The analysis revealed that cracking selectivity was governed not simply by Brønsted acid density, but by Lewis acidity, the LAS/BAS balance and metal-acid coupling, which collectively regulated alkane activation, olefinic-intermediate transformation and secondary cracking probability. Guided by these insights, Zn-incorporated Y zeolites with tunable ZnO/Al_2O_3 molar ratios were synthesized by *in-situ* doping. The optimized catalyst achieved 60.2% selectivity toward jet-fuel-range hydrocarbons. Structural, acidity and mechanistic characterizations showed that Zn incorporation could reconstruct defect-associated acid environments and continuously generate Zn-derived Lewis acid sites, establishing a tunable L/B acid network. *In situ* DRIFTS and DFT calculations further demonstrated that Zn-derived Lewis acid sites promoted alkane activation, while Zn-modulated Pt functionality enhanced dehydrogenation-hydrogenation cycling and suppressed excessive cracking. This work revises the Brønsted-acid-centered view of zeolite hydrocracking and establishes Lewis-acid-mediated acid-metal cooperativity as a design principle for jet-fuel-range hydrocarbons.

1. Introduction

Selective hydrocracking of Fischer-Tropsch (FT) wax provides a promising route to jet-fuel-range hydrocarbons, but approaching ideal hydrocracking requires catalysts that preserve primary cracking products before secondary over-cracking occurs [1]. To achieve this level of selectivity, the key steps must be precisely balanced among metal-mediated dehydrogenation-hydrogenation, acid-catalyzed carbenium-ion chemistry and intracrystalline transport [2][2–5]. Although these elementary processes have been extensively investigated, the catalyst descriptors that determine the transition from selective primary cracking to excessive secondary cracking remain unresolved, because acidity, pore architecture, metal functionality and reaction conditions are intrinsically intertwined.

Y zeolites, with three-dimensional 12-membered-ring channels and tunable acidity, represent a key platform for long-chain alkane hydrocracking [6, 7]. Although Brønsted acid sites are generally recognized as the primary active centers because C-C bond cleavage proceeds via carbenium-ion intermediates [7], this conventional view cannot fully explain the substantial differences in cracking behavior and middle-distillate selectivity often observed among catalysts with similar Brønsted acid densities [8]. Such inconsistencies imply that Lewis acidic environments, including defect-associated and heteroatom-induced Lewis acid sites, may play a more fundamental role. By influencing alkane polarization, the lifetime of olefinic intermediates, the likelihood of secondary cracking, and the electronic interactions between metal and support, Lewis acidity may serve as a key descriptor governing hydrocracking performance. Therefore, clarifying whether Lewis acidity is simply a byproduct

of zeolite modification or an intrinsic descriptor that dictates ideal hydrocracking behavior is significantly essential for advancing catalyst development beyond empirical optimization of acidity.

To verify this hypothesis, a catalyst platform is required, in which the Brønsted/Lewis acid balance can be systematically tuned without substantially altering the Y-zeolite framework [9]. Zn incorporation offers such a platform. Incorporation of Zn species can generate Lewis acid sites, modify acid environments associated with framework defects, and influence the acid-metal interactions involved in dehydrogenation-hydrogenation cycles [10–12]. However, the role of Zn in hydrocracking has been largely interpreted empirically [13], with performance improvements often reported without identifying the underlying descriptor-level origins. Moreover, the simultaneous variations of acidity, pore architecture, metal functionality, and reaction conditions make it difficult for conventional experiments alone to disentangle the key descriptors that govern selective hydrocracking. To address this challenge, interpretable machine learning (ML) offers a complementary framework for resolving complex structure-performance relationships in catalytic systems [14, 15]. By extracting nonlinear correlations from multidimensional datasets, ML-assisted analysis can identify the descriptors most strongly associated with catalytic behavior and provide mechanistic insights that are difficult to obtain through conventional experimentation alone.

Herein, we established a database for long-chain alkane hydrocracking over Y-zeolite-based catalysts by integrating descriptors associated with pore architecture, acidity, metal functionality, and reaction conditions. Correlation analysis identified Lewis acidity, the LAS/BAS balance, and acid-metal coupling as the descriptors most strongly associated with middle-distillate selectivity, rather than Brønsted acid density alone. Interpretable machine learning was then employed to translate these coupled catalytic variables into experimentally testable descriptor hypotheses. Guided by the resulting descriptor hierarchy, a series of Zn-incorporated Y zeolites with tunable ZnO/Al_2O_3 molar ratios were synthesized via *in situ* doping and subsequently loaded with Pt. Hydrocracking tests using n-docosane and FT wax demonstrated that the optimized Pt/ZnY catalyst effectively directed product distribution toward jet-fuel-range hydrocarbons. Mechanistic studies further revealed that Zn incorporation reconstructed defect-associated acidic environments, continuously generated Zn-derived Lewis acid sites, and established a tunable Lewis/Brønsted acid network. Combined *in situ* DRIFTS measurements and DFT calculations showed that Zn-derived Lewis acid sites facilitated alkane activation, while Zn-modulated Pt functionality promoted efficient dehydrogenation-hydrogenation cycling and suppressed secondary over-cracking. Collectively, these findings shift the design paradigm of zeolite hydrocracking from empirical Brønsted-acid optimization toward descriptor-guided engineering of Lewis-acid-mediated acid-metal cooperation for selective FT-wax hydrocracking to jet-fuel-range hydrocarbons.

2. Results and discussions

Pearson and Spearman correlation analyses were firstly conducted to evaluate statistical associations among descriptors in the Y-zeolite hydrocracking database and their relationships with conversion and cracking selectivity (**Fig. S1**). The correlation heatmaps revealed pronounced collinearity among pore-

structure, acidity, metal-function and reaction-condition descriptors, indicating that the catalytic behavior of Y-zeolite-based hydrocracking catalysts cannot be interpreted from isolated variables alone. This descriptor coupling justified the construction of catalytically meaningful derived descriptors and the use of machine-learning models to capture multivariable and nonlinear structure-performance relationships. Accordingly, multiple linear and nonlinear models were trained and compared for conversion and cracking selectivity prediction (**Fig. S1 (c-h)**). The superior performance of nonlinear ensemble models confirmed the strongly coupled nature of the hydrocracking dataset. Histogram gradient boosting provided the best prediction for conversion (CV R^2= 0.920, RMSE = 8.677), whereas extra trees gave the highest accuracy for cracking selectivity (CV R^2= 0.920, RMSE = 9.026). These results demonstrated that hydrocracking over Y zeolites was governed by nonlinear interactions among acidity, pore architecture, metal functionality and reaction conditions. Permutation importance and SHAP analyses were therefore further applied to interpret the trained models and identify the descriptors responsible for conversion and selectivity control (Fig. 1).

After excluding reaction-condition descriptors (including LHSV, temperature, and derived temperature/LHSV), the most important catalyst-intrinsic variables for conversion were mainly acidity-related descriptors, such as L/B ratio, total acidity and total acid/S_{BET} (surface-normalized density of accessible acid sites) than pore-structure descriptors such as V_{micro} and S_{BET}. Such ranking indicated that intrinsic differences in conversion over Y zeolites were primarily governed by acid-type distribution and effective acid-site density. Although process-level variables (temperature, feed property, conversion, and derived conversion-related descriptors) remained important, cracking selectivity was governed mainly by Pt loading, Lewis acidity, and LAS/BAS balance. These results indicate that conversion mainly reflects the availability and type of acid sites, whereas cracking selectivity is more sensitive to Lewis acidity, acid-metal coupling and hydrogenation-dehydrogenation functionality.

The key outcome of the model interpretation was a descriptor shift from Brønsted-acid density to Lewis-acid-mediated acid-metal cooperativity for selectivity control. The stronger contribution of LAS-related descriptors than BAS suggested that selective hydrocracking was not governed solely by BAS-mediated C-C bond cleavage, but also by LAS-assisted hydrocarbon activation, intermediate stabilization and metal-mediated dehydrogenation-hydrogenation cycling. Accordingly, catalyst design should prioritize coordinated regulation of Lewis/Brønsted acid distribution and metal functionality rather than relying only on increasing total acidity or pore accessibility. On this basis, *in situ* Zn-modified Y zeolite catalysts were further prepared and evaluated to validate this descriptor-guided regulation strategy for long-chain alkane hydrocracking and to assess its effects on catalytic activity and cracking selectivity.

Figure 2 summarizes the selective hydrocracking performance of Pt/(Y + ASA) and Pt/(xZnY + ASA) (x = 0.1–0.4) catalysts. Although n-C_{22} conversion increased continuously with temperature, C_9-C_{17} yield and selectivity exhibited volcano-shaped profiles, reaching maxima at 380°C because of competition between primary hydrocracking and consecutive cleavage of middle-distillate products (Fig. 2**(a-c)**). Parent Pt/(Y + ASA) was more active, whereas Pt/(0.2ZnY + ASA) afforded the highest C_9-C_{17} yield and

selectivity of 37.8% and 60.2%, respectively, exceeding those of the parent catalyst by 2.8 and 12.8 percentage points. Consistently, Pt/(0.2ZnY + ASA) produced a nearly symmetric, bell-shaped carbon-number distribution centered in the jet-fuel range and markedly suppressed the formation of over-cracked C_3-C_8 products (Fig. 2**(d)**). The absence of C_1-C_2 products and the minimum fragment size of C_3 were consistent with the classical bifunctional pathway involving Pt-mediated dehydrogenation, BAS-mediated carbenium-ion formation and rearrangement, and selective A/B/C-type β-scission, whereas D-type cleavage through unstable primary carbenium ions was kinetically disfavored (**Fig. S2**) [16]. FT wax hydrocracking further demonstrated practical applicability: Pt/(0.2ZnY + ASA) suppressed light-gas and gasoline formation while delivering a jet-fuel yield of 26.3% and selectivity of 63.6%, a 13.7-percentage-point increase over Pt/(Y + ASA) (Fig. 2**(e-f)**). Benchmarking against representative literature catalysts confirmed its superior performance (57.8% conversion, 60.2% cracking selectivity; Fig. 2**(g)** and **Table S2**). Transferability of the Lewis-Brønsted acid balance descriptor was confirmed using Co-modified Y zeolites. Pt/(0.3CoY + ASA) achieved the optimal performance in the Co series (C_9-C_{17} yield 36.9%, selectivity 51.8%; Fig. 2**(h-i)** and **Fig. S3(a)**), with NH_3-TPD and Py-IR analyses indicating an increased L/B ratio (**Fig. S3(b-d)**, **Table S1**). Catalyst stability and coke-resistance tests showed that Pt/(0.2ZnY + ASA) maintained stable conversion and selectivity with minimal carbon deposition (3.48 wt%), whereas higher Zn loadings led to increased coke formation and Pt agglomeration (**Figs. S4-5**, **Table S3**), highlighting its strong industrial applicability. Collectively, these results experimentally validated the machine-learning prediction that selective middle-distillate production was governed by an optimized Lewis-Brønsted acid balance rather than by maximizing Brønsted acidity alone.

Given the pronounced differences in hydrocracking performance among Zn-modified catalysts, structural properties were first examined to evaluate possible structure-performance correlations **(Figs. S6-7**, **Table S4)**. All xZnY zeolites retained the characteristic FAU topology (ICDD PDF#77-1549), whereas ZnO/Al_2O_3 ratios above 0.4 caused pronounced framework degradation; therefore, compositions of 0.1–0.4 were selected for systematic investigation **(Fig. S6(a))**. Zn incorporation increased the exposure of the [111] and [220] crystal planes, shifted the low-angle reflections to lower 2θ values, and enlarged the crystallites from 131 to 201 nm, indicating altered crystal growth and unit-cell expansion associated with the longer Zn-O bonds (Zn-O bonds (1.9 Å) relative to Al-O (1.7 Å) and Si-O (1.6 Å) [17]. At $ZnO/ Al_2O_3 \leq$ 0.2, pore volumes and average pore size increased, whereas higher Zn loadings reduced these parameters, likely because of partial blockage by oligomeric Zn species. Although no large ZnO aggregates were detected, small surface ZnO_x domains cannot be excluded, necessitating complementary spectroscopic analysis of Zn speciation.

Zn incorporation markedly altered the framework composition and local chemical environment of Y zeolites. To quantify the migration of framework Si and Al, the dealumination rate (D_{Al}) and desilication rate (D_{Si}) $\left(D_{Al/Si} = \frac{n_{Al/Si,Y} - n_{Al/Si,xZnY}}{n_{Al/Si,Y}}\right)$ were defined relative to the parent Y zeolite, where n_{Al} and n_{Si} represent the molar amounts of Al and Si, respectively. As shown in Fig. 3**(b)**, Zn incorporation progressively increased the SiO_2/Al_2O_3 ratio through preferential dealumination, with Al removal exceeding Si loss by 2.6-3.8-fold.

Notably, D_{Al}/D_{Si} reached a maximum of 3.8 at $n(ZnO)/n(Al_2O_3)$ = 0.2, identifying a distinct compositional turning point in the framework evolution. Complementary FT-IR analysis revealed systematic redshifts of local T-O-T bonding environment without disruption of the fundamental FAU topology (**Fig. S8**). These spectral changes did not, however, establish direct crystallographic substitution of framework Al by Zn, but instead indicated local framework reconstruction involving Zn-O-Si interactions and distortion of neighboring Si-O-Al linkages. Together, these results demonstrated that Zn-induced redistribution of framework elements and reconstruction of the local coordination environment, rather than changes in crystallinity or porosity alone, were central to the catalytic behavior, motivating further analysis of Zn speciation and defect evolution.

UV-vis, OH-FTIR, O 1s XPS, and solid-state NMR collectively elucidated the Zn-speciation evolution and defect-acid reconstruction in xZnY zeolites (Fig. 3**(c-f)**). UV-vis diffuse reflectance spectra showed an intense ligand-to-metal charge-transfer band at approximately 220 nm, assigned to highly dispersed Zn^{2+} species in tetrahedral or pseudo-tetrahedral coordination, together with a progressively intensified shoulder near 280 nm associated with defect-bound Zn species, including $[ZnOH]^+$ and highly dispersed Zn-O-Zn moieties [18]. The absence of the characteristic absorption of bulk ZnO near 375 nm [9] excluded the formation of large ZnO particles, although nanoscale ZnO_x domains at high Zn loadings cannot be completely ruled out. These observations indicated a gradual transition from isolated, framework-associated Zn species toward increasingly complex extra-framework Zn coordination environments with increasing Zn content. Typically, upon *in-situ* incorporation of Zn^{2+} species, partial substitution of framework Al by Zn induced framework reorganization, while extra-framework Zn species evolved sequentially from Zn^{2+} to $[ZnOH]^+$ and $[Zn\text{-}O\text{-}Zn]^{2+}$, eventually forming ZnO_x clusters [19] (**Fig. S9**).

The corresponding evolution of hydroxyl and oxygen environments revealed a distinct compositional threshold at ZnO/Al_2O_3=0.2. OH-FTIR (Fig. 3**(e)**) showed that the concentrations of Si-OH (3745 cm^{-1}), Al-OH (3650–3680 cm^{-1}), and bridging Si-OH-Al groups (3610 cm^{-1}) [20] initially decreased and reached minima at this composition, whereas $[ZnOH]^+$ species (3630 cm^{-1}) progressively accumulated. Quantitative deconvolution of O 1s XPS spectra (**Table S5**) provided a semi-quantitative view of Zn-species evolution. Si-OH and Al-OH groups, generally regarded as defect sites in zeolites[20], exhibited similar non-monotonic behavior. At low Zn loadings, both Si-OH and Al-OH species decreased, indicating consumption of defect sites. At higher Zn loadings, defect sites were regenerated due to disruption of framework equilibrium caused by excessive Zn incorporation. Si-O-Si species exhibited an inverse trend relative to Si-OH groups, indicating that Zn species preferentially interacted with silanol groups, promoting their condensation into Si-O-Si species and incorporation into the framework as Si-O-Zn linkages. Thus, the minimum in hydroxyl concentration at ZnO/Al_2O_3 = 0.2 marks the crossover from defect healing to defect regeneration.

Combined OH-FTIR and O 1s XPS analyses were used to track the evolution of Si-OH-Al. Based on these observations, a mechanistic model describing Zn coordination environments and Zn-framework

interactions was proposed (Fig. 3**(d)**), in which step ① represented framework substitution, while steps ②-④ described the evolution of extra-framework Zn species. Isolated Zn^{2+} cations, $[ZnOH]^+$ species, and binuclear $[Zn\text{-}O\text{-}Zn]^{2+}$ dimers exhibited dehydrogenation activity, whereas ZnO_x aggregates (n > 2) and bulk ZnO clusters remained inactive [21–23]. At $ZnO/Al_2O_3 < 0.2$, the decrease in Si-OH-Al groups was mainly attributed to ion exchange between Zn^{2+} species and BASs (Eq. 2), in which one Zn^{2+} cation compensated two framework negative charges and consumed two Brønsted acid protons. Although framework Si-O-Zn may create new acid environments, this contribution was outweighed at low Zn loading by the consumption and masking of pre-existing BAS through Zn^{2+} exchange. At higher Zn loadings, the transformation of Zn^{2+} into $[ZnOH]^+$ and $[Zn\text{-}O\text{-}Zn]^{2+}$ (steps ③-④) released protons, leading to regeneration of BASs. This behavior identified ZnO/Al_2O_3=0.2 as a critical transition point governing acid site evolution.

^{29}Si and ^{27}Al MAS NMR further resolved the atomic-scale framework reconstruction underlying this transition (Figs. 3**(g-h) & S11, Tables S6-8**). At $ZnO/Al_2O_3 \leq 0.2$, the fractions of Si(4Si) and Zn-associated Si environments increased, while defect-rich Q3Si/Q2Si (Si(1Me/Si(2Me)) environments decreased, indicating that Zn incorporation promoted silanol condensation. Meanwhile, Si(nAl) units underwent substantial reorganization. Si(4Al) decreased, whereas Si(1-3Al) species increased, suggesting redistribution of tetrahedral Al from clustered to more dispersed environments. In parallel, Al-OH species, distorted tetrahedral Al, pentacoordinated Al, and extra-framework Al declined, while stable tetrahedral framework Al increased. These results indicated that Zn incorporation drove Al into thermodynamically more stable framework positions. Although the total Al content gradually decreased, tetrahedral framework Al reached a maximum at ZnO/Al_2O_3 = 0.2, demonstrating pronounced framework reorganization rather than simple dealumination. Upon further increasing Zn loading, the structural evolution reversed. The fraction of Si(4Si) decreased, while less-connected Si environments became more prevalent. Consistent with the ^{29}Si MAS NMR results, Si(3Al) and Si(4Al) environments progressively transformed into Si(1Al) and Si(2Al) species. Simultaneously, pentacoordinated Al and Al-OH species reappeared, indicating localized desilication, Al redistribution, and regeneration of Si-OH and Al-OH defects. This behavior agreed with the OH-FTIR and O 1s XPS results. These transformations alter local charge compensation, promote proton redistribution, and reconstruct the Brønsted and Lewis acid environments.

^1H MAS NMR provided direct evidence for Zn-induced redistribution of hydroxyl and Brønsted acid environments (**Fig. S12**, **Table S9**). Brønsted proton intensity decreased at $ZnO/Al_2O_3 \leq 0.2$ and increased thereafter. This non-monotonic evolution was consistent with the variation of BAS observed by pyridine-adsorbed FT-IR. A uantitative correlation of BAS evolution with the Zn/BAS ratio was established (Fig. 4**(a)**). Extra-framework Zn^{2+} species exchanged with two BASs, while $[ZnOH]^+$ and $[Zn\text{-}O\text{-}Zn]^{2+}$ species interacted with BAS in an approximately 1:1 stoichiometric manner [23]. A parameter K was introduced to describe the net change in BAS relative to Zn incorporation. At $ZnO/Al_2O_3 \leq 0.2$ (Zn/BAS = 2.22/5.08), K > 0 indicated net consumption of BAS. Notably, K values exceeded the stoichiometric limit

(> 2) due to selective dealumination and partial desilication that removed Al-associated BAS and defect hydroxyls. As ZnO/Al_2O_3 increased from 0.1 to 0.2, K decreased from 5.45 to 3.19, indicating a reduced rate of BAS consumption driven by extra-framework Zn evolution. Above ZnO/Al_2O_3>0.2, K became negative, indicating significant recovery of BAS as Zn species transformed into $[ZnOH]^+$, $[Zn\text{-}O\text{-}Zn]^{2+}$, and eventually ZnO_x, accompanied by framework Al redistribution and defect rehydroxylation. Resonances near 6.8 ppm, attributed to water on Lewis sites or residual ammonium, were excluded from analysis [24, 25]. NH_3-TPD and Py-IR analyses[9] revealed a V-shaped evolution of acid properties with increasing Zn loading, where total BAS density initially decreased and then recovered, reaching a minimum at 0.2ZnY, while LAS density increased continuously. The rise in weak BAS correlated with more dispersed Al environments (Si(2Al) and Si(3Al)), and Isolated Zn^{2+}, $[ZnOH]^+$, and $[Zn\text{-}O\text{-}Zn]^{2+}$ all functioned as LAS centers [26], promoting carbocation formation, rearrangement, and hydrogen-transfer reactions. This behavior indicated that acid site evolution originated from defect-reconstruction-driven structural changes induced by Zn incorporation. 0.2ZnY achieving the lowest BAS density together with the most balanced L/B ratio that maximized primary β-scission while suppressing secondary cracking. Collectively, these results demonstrated that Zn-induced defect-acid network reconstruction enabled dynamic regulation of L/B ratio and Zn functionality, establishing an optimal catalytic state.

Enhanced dehydrogenation functionality is particularly important for bifunctional hydrocracking, since olefinic intermediates generated via initial alkane activation serve as essential precursors for Brønsted-acid-mediated β-scission. *In situ* DRIFTS using n-dodecane as a probe revealed that Zn incorporation markedly altered both hydrocarbon adsorption and surface reaction pathways (Fig. 5**(d-i)**). All supports and Pt-loaded catalysts exhibited characteristic C-H stretching vibrations of $-CH_2-$ and terminal $-CH_3$ groups [27]. Although 0.2ZnY showed slightly weaker initial adsorption than Y, consistent with its lower BAS density and reconstructed hydroxyl environment, the slower decay of alkyl C-H bands indicated stronger stabilization of surface hydrocarbons by Zn-derived Lewis acid sites through C-H polarization. After Pt loading, Pt/0.2ZnY displayed substantially stronger hydrocarbon adsorption than Pt/Y, indicating that Zn-induced interfacial reconstruction enhanced hydrocarbon enrichment at catalytically relevant sites through optimized metal-support interactions. More importantly, a new band near 3100 cm^{-1}, assigned to olefinic = C-H stretching, emerged only over the Pt-containing catalysts. Its earlier appearance and higher intensity over Pt/0.2ZnY demonstrated accelerated Pt-mediated alkane dehydrogenation rather than simple desorption. This enhancement originates from the cooperative interaction between Zn-derived Lewis acid sites, which polarize alkane C-H bonds, and Zn-induced defect-acid reconstruction, which optimizes Pt dispersion and metal–support electronic interactions. Consequently, Pt/0.2ZnY generates unsaturated intermediates more efficiently and feeds them more rapidly into the subsequent protonation and β-scission sequence. DFT calculations **(Fig. S13**, **Table S17)** further clarified the molecular origin of this behavior. Adsorption became progressively stronger with increasing alkane chain length on both Y and ZnY confirming stronger interactions between longer hydrocarbons and zeolitic active sites. Notably, Zn incorporation substantially enhanced adsorption of long-chain alkanes, with adsorption energies for ZnY decreasing from − 0.06 eV (C_6) to -1.65 eV (C_{12}), compared with − 0.11 to -0.69 eV for the parent Y model. Thus, Zn-derived Lewis acid sites preferentially

stabilize long-chain reactants and modify the local electronic environment surrounding neighboring Brønsted acid sites. This preferential adsorption increases the probability of primary activation and β-scission of long-chain hydrocarbons, while decreasing the competitive occupation of active sites by shorter cracked products. The resulting adsorption-energy differentiation suppresses consecutive cracking and provides a mechanistic basis for the enhanced C_9-C_{17} selectivity of Pt/0.2ZnY. Collectively, Zn-induced LAS modified the local electronic environment of neighboring BAS and influenced the adsorption configurations of olefinic intermediates, branched carbenium ions, and cracking intermediates, thereby regulating cracking depth.

Zn incorporation induced defect-mediated reconstruction of the support, which controlled Pt dispersion and particle size (Fig. 5**(a-c), Fig. S14, Table S12**) through evolution of Zn species and regenerated BAS. Notably, HAADF-STEM elemental mapping of Pt/(0.2ZnY + ASA) (Fig. 5**(c)**) revealed a highly overlapped and homogeneous spatial distribution of Pt and Zn species, indicating strong interfacial interactions between Pt nanoparticles and Zn-derived anchoring sites. At ZnO/Al_2O_3=0.2, evolution of Zn species generated multiple effective anchoring environments, including $[ZnOH]^+$, $[Zn\text{-}O\text{-}Zn]^{2+}$, regenerated BASs, and defect-associated hydroxyl groups. These collectively stabilized Pt nanoparticles (2.61 nm) with predominant {111} facets, maximizing accessible metallic active sites and enhancing alkane (de)hydrogenation [28]. Below this threshold, BAS depletion by extra-framework Zn^{2+} reduced anchoring efficiency, leading to Pt aggregation and lower dispersion, whereas higher Zn loadings (> 0.2) introduced surface heterogeneity and weakly interacting hydroxyls, diminishing Pt stabilization despite increased defect density. These results demonstrated that Pt dispersion was governed by the nature and effectiveness of Zn-mediated anchoring sites rather than their absolute number.

H_2-TPR (**Fig. S15, Table S13**) and DFT analyses (**Fig. S16**) indicated that Zn incorporation optimized Pt reducibility and metal-acid synergy. The electron-donating effect of Zn weakened newly formed Pt-O-Zn bonds relative to Pt-O-Al linkages, lowering metal-support interaction (MSI) strength and shifting the Pt reduction peaks from 470–510 °C to lower temperatures. DFT and differential charge analysis showed decreased surface electron density, reduced binding energy (-18.62 eV to -19.47 eV), and shortened Pt-O bonds (2.09 Å to 2.02 Å), reflecting weaker Pt anchoring. This weakened MSI promoted higher Pt dispersion and smaller nanoparticles, consistent with TEM and CO chemisorption data. Among the series, 0.2ZnY zeolite catalyst exhibited the lowest BAS and the highest n_{Pt}/n_A ratio, resulting in optimal Pt dispersion and reducibility and thus the most favorable metal-acid synergy.

By transitioning from the acid-dominated configuration of Pt/Y catalyst to the metal-enriched and functionally balanced architecture of Pt/0.2ZnY catalyst (Fig. 5**(j)**), the resulting catalyst achieved not only enhanced activity but also superior selectivity [29]. n-C_{22} primarily underwent single-event cracking, on Pt/(0.2ZnY + ASA) catalyst. Pt^0 and Zn sites (isolated Zn^{2+} cations, $[ZnOH]^+$ species, and binuclear $[Zn\text{-}O\text{-}Zn]^{2+}$ dimers) activate alkane C-H bonds via LAS, generating olefinic intermediates that rapidly migrate to neighboring BAS for protonation and β-scission [26]. Competitive adsorption on reduced BAS density limited molecules to single cracking events before hydrogenation at Pt sites [30]. Zn-mediated

defect generation, silanol nests, and ≡ Si-O-Zn moieties anchor highly dispersed Pt nanoparticles, enhancing dehydrogenation-hydrogenation functionality. Spatial proximity between Pt and BAS promoted rapid hydrogen transfer and suppresses secondary cracking, maximizing C_9-C_{17} formation. Given the intrinsically high reactivity of long-chain n-C_{22} Brønsted acidity must therefore be carefully moderated to suppress over-cracking, as established in previous studies [8, 31]. Excessive Brønsted acidity in the parent Y zeolite prolonged olefin residence on acid sites and promoted secondary cracking. Simultaneously, reduced Pt dispersion impeded timely product desorption. These combined effects diminished C_9-C_{17} yield and selectivity.

Collectively, these results demonstrated that Zn incorporation regulated hydrocracking behavior not only through reconstruction of the defect-acid network, but also by reconfiguring the alkane activation and hydrogenation-dehydrogenation functionality of the bifunctional catalyst. The resulting catalyst therefore achieved an optimal bifunctional balance, in which efficient alkane activation, single cracking events, and timely hydrogenation of reactive intermediates collectively redirected the hydrocracking network toward the ideal regime dominated by primary cracking. Notably, these experimental and computational results directly validated the interpretable machine-learning predictions, confirming that hydrocracking selectivity over Y-based catalysts is governed by the coupled interplay among acidity, Lewis-assisted alkane activation, metal-mediated dehydrogenation capability, and metal-acid balance rather than by any single structural descriptor.

3. Conclusion

In this work, a descriptor-guided strategy for approaching ideal hydrocracking of Fischer-Tropsch wax over Y-zeolite-based bifunctional catalysts has been developed. Interpretable machine learning revealed that cracking selectivity was governed not by Brønsted acid density alone, but by Lewis acidity, LAS/BAS balance and metal-acid cooperativity. Guided by this descriptor shift, Zn-incorporated Y zeolites were designed to reconstruct defect-associated acid environments and generate Zn-derived Lewis acid sites, thereby establishing a tunable Lewis/Brønsted acid network. The optimized Pt/(0.2ZnY + ASA) catalyst achieved the highest C_9-C_{17} yield and selectivity in both n-C_{22} and FT wax hydrocracking. Mechanistic evidence from spectroscopy, *in situ* DRIFTS and DFT calculations showed that Zn-derived Lewis acid sites promoted alkane activation and long-chain hydrocarbon adsorption, while Zn-modulated Pt functionality facilitated hydrogenation-dehydrogenation cycling and suppressed secondary over-cracking. These findings challenge the conventional Brønsted-acid-centered interpretation of zeolite hydrocracking and establish Lewis-acid-mediated acid-metal cooperativity as a unifying principle for controlling selectivity in complex bifunctional catalytic systems.

Declarations

Acknowledgements

The work was supported by National Key R&D Program of China (No.2022YFA1503400), State Key Laboratory of Heavy Oil Processing, China University of Petroleum (No.WX20250146) and Science Foundation of China University of Petroleum, Beijing (No. 2462023QNXZ018).

References

1. Becker PJ, Celse B, Guillaume D, Costa V, Bertier L, Guillon E, Pirngruber G (2016) A continuous lumping model for hydrocracking on a zeolite catalysts: model development and parameter identification. Fuel 164:73–82
2. Bouchy C, Hastoy G, Guillon E, Martens JA (2009) Fischer-Tropsch waxes upgrading via hydrocracking and selective hydroisomerization, Oil & Gas Science and Technology-Revue de l'IFP 64 91–112
3. Regali F, Liotta LF, Venezia AM, Boutonnet M, Järås S (2014) Hydroconversion of n-hexadecane on Pt/silica-alumina catalysts: Effect of metal loading and support acidity on bifunctional and hydrogenolytic activity. Appl Catal A 469:328–339. https://doi.org/10.1016/j.apcata.2013.09.048
4. Weitkamp J, Jacobs PA, Martens JA (1983) Isomerization and hydrocracking of C9 through C16 n-alkanes on Pt/HZSM-5 zeolite. Appl Catal 8:123–141
5. Mabaleha SS, Delo A, Kalita P (2024) Secondary cracking suppression over zeolite-based catalysts: A review. Renew Sustain Energy Rev 203:114789. https://doi.org/10.1016/j.rser.2024.114789
6. Degnan TF Jr (2003) The implications of the fundamentals of shape selectivity for the development of catalysts for the petroleum and petrochemical industries. J Catal 216:32–46
7. Mabaleha SS, Delo A, Kalita P (2024) Secondary cracking suppression over zeolite-based catalysts: A review. Renew Sustain Energy Rev 203:114789. https://doi.org/10.1016/j.rser.2024.114789
8. Shao F, Guo F, Bai T, Xu Z, Yang H, Kang W, Zhou Y, Huang W, Wang G, Wei Q (2026) Synthesis of hierarchical nano-Y zeolite supported Pt catalyst for efficient hydrocracking of Fischer–Tropsch wax to jet fuel. Fuel 407:137428
9. Parmar D, Mallette AJ, Linares N, Saslow SA, Terlier T, Strohm JJ, Barber LP, Dai H, García-Martínez J, Rimer JD (2023) Direct Synthesis of Highly Siliceous ZnO-FAU Zeolite with Enhanced Performance in Hydrocarbon Cracking Reactions. ACS Mater Lett 5:202–208. https://doi.org/10.1021/acsmaterialslett.2c00978
10. Yang Z, Liu Y, Zhao J, Gou J, Sun K, Liu C (2017) Zinc-modified Pt/SAPO-11 for improving the isomerization selectivity to dibranched alkanes. Chin J Catal 38:509–517. https://doi.org/10.1016/S1872-2067(17)62755-4
11. Tu C, Fan H, Wang D, Rui N, Du Y, Senanayake SD, Xie Z, Nie X, Chen JG (2022) CO2-assisted ethane aromatization over zinc and phosphorous modified ZSM-5 catalysts. Appl Catal B 304:120956. https://doi.org/10.1016/j.apcatb.2021.120956
12. Chen G, Xie Z, Xiang Y (2025) Tuning the Reactivity of Zn Sites in HZSM-5 Zeolite for Light Alkane Activation. ACS Catal 15:3722–3730. https://doi.org/10.1021/acscatal.4c06464

13. Wang L, Sang S, Meng S, Zhang Y, Qi Y, Liu Z (2007) Direct synthesis of Zn-ZSM-5 with novel morphology. Mater Lett 61:1675–1678
14. Wang X, Qi J, Wan M, Li F, Yuan J, Liu Z, Zheng A (2026) Harnessing confinement effect and interpretable machine learning to predict alkane diffusion in zeolite catalysts. Nat Commun. https://doi.org/10.1038/s41467-026-71698-0
15. Huang M, Wang S, Zhu H (2023) A comprehensive machine learning strategy for designing high-performance photoanode catalysts. J Mater Chem A 11:21619–21627. https://doi.org/10.1039/D3TA04148D
16. Schweitzer J-M, Rey J, Bignaud C, Bučko T, Raybaud P, Moscovici-Mirande M, Portejoie F, James C, Bouchy C Multi-scale Modeling as a Tool for the Prediction of Catalytic Performances: the Case of n-Heptane Hydroconversion in a Large Pore Zeolite, (n.d.).
17. Mallette AJ, Hong S, Freeman EE, Saslow SA, Mergelsberg S, Motkuri RK, Neeway JJ, Mpourmpakis G, Rimer JD (2022) Heteroatom Manipulation of Zeolite Crystallization: Stabilizing Zn-FAU against Interzeolite Transformation. JACS Au 2:2295–2306. https://doi.org/10.1021/jacsau.2c00325
18. Koike N, Iyoki K, Wang B, Yanaba Y, Elangovan SP, Itabashi K, Chaikittisilp W, Okubo T (2018) Increasing the ion-exchange capacity of MFI zeolites by introducing Zn to aluminosilicate frameworks. Dalton Trans 47:9546–9553. https://doi.org/10.1039/C8DT01391H
19. Tu C, Wang H, Zhai W, Liu C, Huang W, Li W (2025) Defect engineering of zinc-modified ZSM-5 zeolite catalysts for efficient aromatic synthesis from ethane and CO2. Chem Eng J 513:162967. https://doi.org/10.1016/j.cej.2025.162967
20. Xing A, Zhang N, Yuan D, Liu H, Sang Y, Miao P, Sun Q, Luo M (2019) Relationship between Acidity, Defective Sites, and Diffusion Properties of Nanosheet ZSM-5 and Its Catalytic Performance in the Methanol to Propylene Reaction. Ind Eng Chem Res 58:12506–12515. https://doi.org/10.1021/acs.iecr.9b00325
21. Nozik D, Tinga FMP, Bell AT (2021) Propane Dehydrogenation and Cracking over Zn/H-MFI Prepared by Solid-State Ion Exchange of $ZnCl_2$, ACS Catal. 11:14489–14506. https://doi.org/10.1021/acscatal.1c03641
22. Yuan Y, Lobo RF (2023) Zinc Speciation and Propane Dehydrogenation in Zn/H-ZSM-5 Catalysts. ACS Catal 13:4971–4984. https://doi.org/10.1021/acscatal.2c05898
23. Almutairi SMT, Mezari B, Magusin PCMM, Pidko EA, Hensen EJM (2012) Structure and Reactivity of Zn-Modified ZSM-5 Zeolites: The Importance of Clustered Cationic Zn Complexes. ACS Catal 2:71–83. https://doi.org/10.1021/cs200441e
24. Qin Z, Shen B, Yu Z, Deng F, Zhao L, Zhou S, Yuan D, Gao X, Wang B, Zhao H, Liu H (2013) A defect-based strategy for the preparation of mesoporous zeolite Y for high-performance catalytic cracking. J Catal 298:102–111. https://doi.org/10.1016/j.jcat.2012.11.023
25. Andreev AS, Livadaris V (2017) Characterization of Catalytic Materials through a Facile Approach to Probe OH Groups by Solid-State NMR. J Phys Chem C 121:14108–14119. https://doi.org/10.1021/acs.jpcc.7b02283

26. Gabrienko AA, Arzumanov SS, Toktarev AV, Danilova IG, Prosvirin IP, Kriventsov VV, Zaikovskii VI, Freude D, Stepanov AG (2017) Different Efficiency of Zn^{2+} and ZnO Species for Methane Activation on Zn-Modified Zeolite. ACS Catal 7:1818–1830. https://doi.org/10.1021/acscatal.6b03036
27. Liu Z, Mei J, Kong X, Chen Z, Li D, Li H, Wang C, Gong Y, Xu C, Wang X (2025) Rational design of hierarchical porous structure of ZSM-22 for boosting high-efficiency selective hydrogenation of oleic acid to jet fuel. Chem Eng J 507:160585. https://doi.org/10.1016/j.cej.2025.160585
28. Wang Y, Tao Z, Wu B, Xu J, Huo C, Li K, Chen H, Yang Y, Li Y (2015) Effect of metal precursors on the performance of Pt/ZSM-22 catalysts for n -hexadecane hydroisomerization. J Catal 322:1–13. https://doi.org/10.1016/j.jcat.2014.11.004
29. Samad JE, Blanchard J, Sayag C, Louis C, Regalbuto JR (2016) The controlled synthesis of metal-acid bifunctional catalysts: The effect of metal: acid ratio and metal-acid proximity in Pt silica-alumina catalysts for n-heptane isomerization. J Catal 342:203–212
30. Oda A, Ohkubo T, Yumura T, Kobayashi H, Kuroda Y (2017) Why do zeolites induce an unprecedented electronic state on exchanged metal ions? Phys Chem Chem Phys 19:25105–25114. https://doi.org/10.1039/c7cp02669b
31. Hanaoka T, Miyazawa T, Shimura K, Hirata S (2015) Jet fuel synthesis from Fischer–Tropsch product under mild hydrocracking conditions using Pt-loaded catalysts. Chem Eng J 263:178–185. https://doi.org/10.1016/j.cej.2014.11.042

Figures

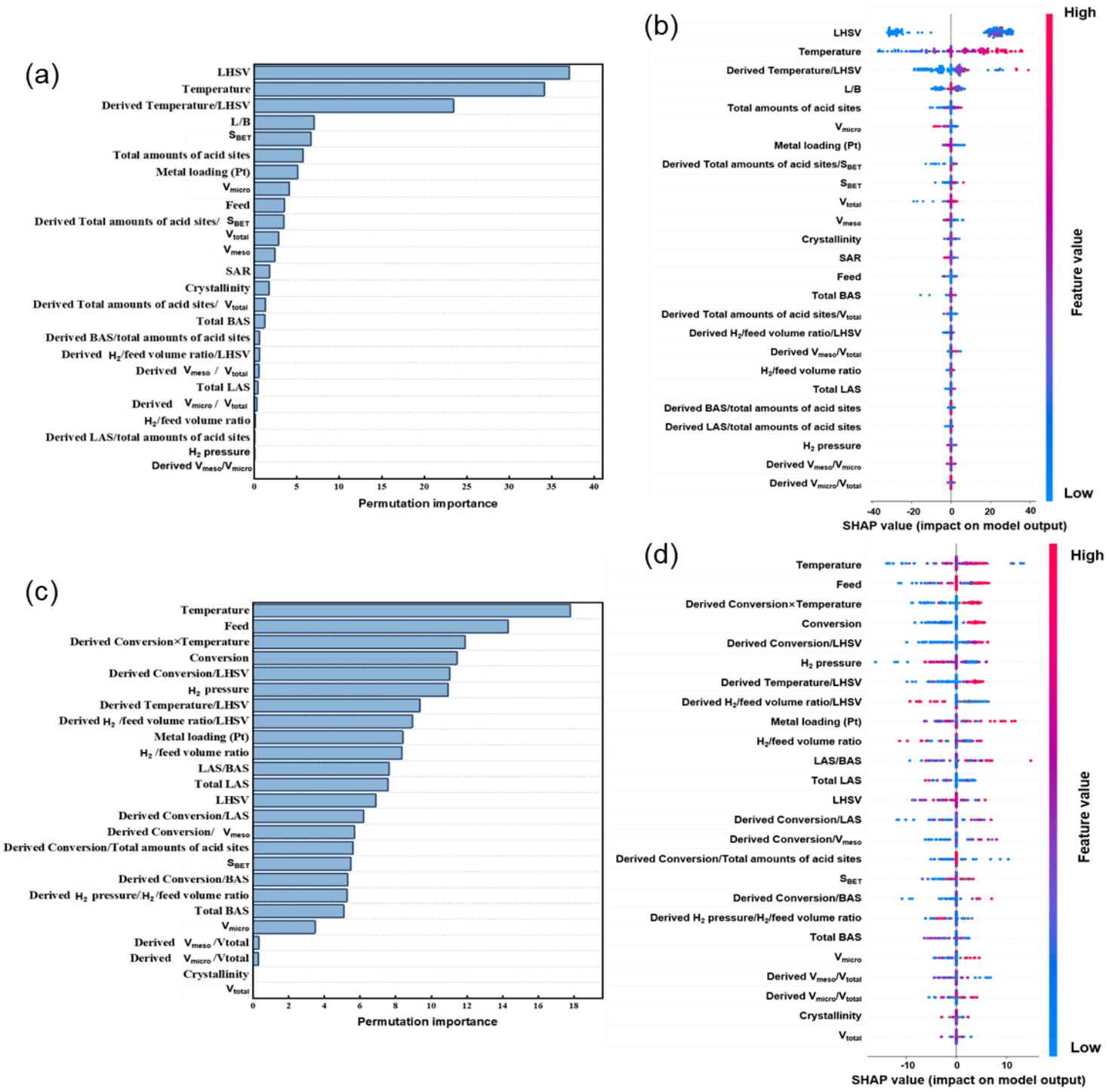


Figure 1

Permutation importance for (a) conversion and (c) cracking selectivity; SHAP summary plots for (b) conversion and (d) cracking selectivity.

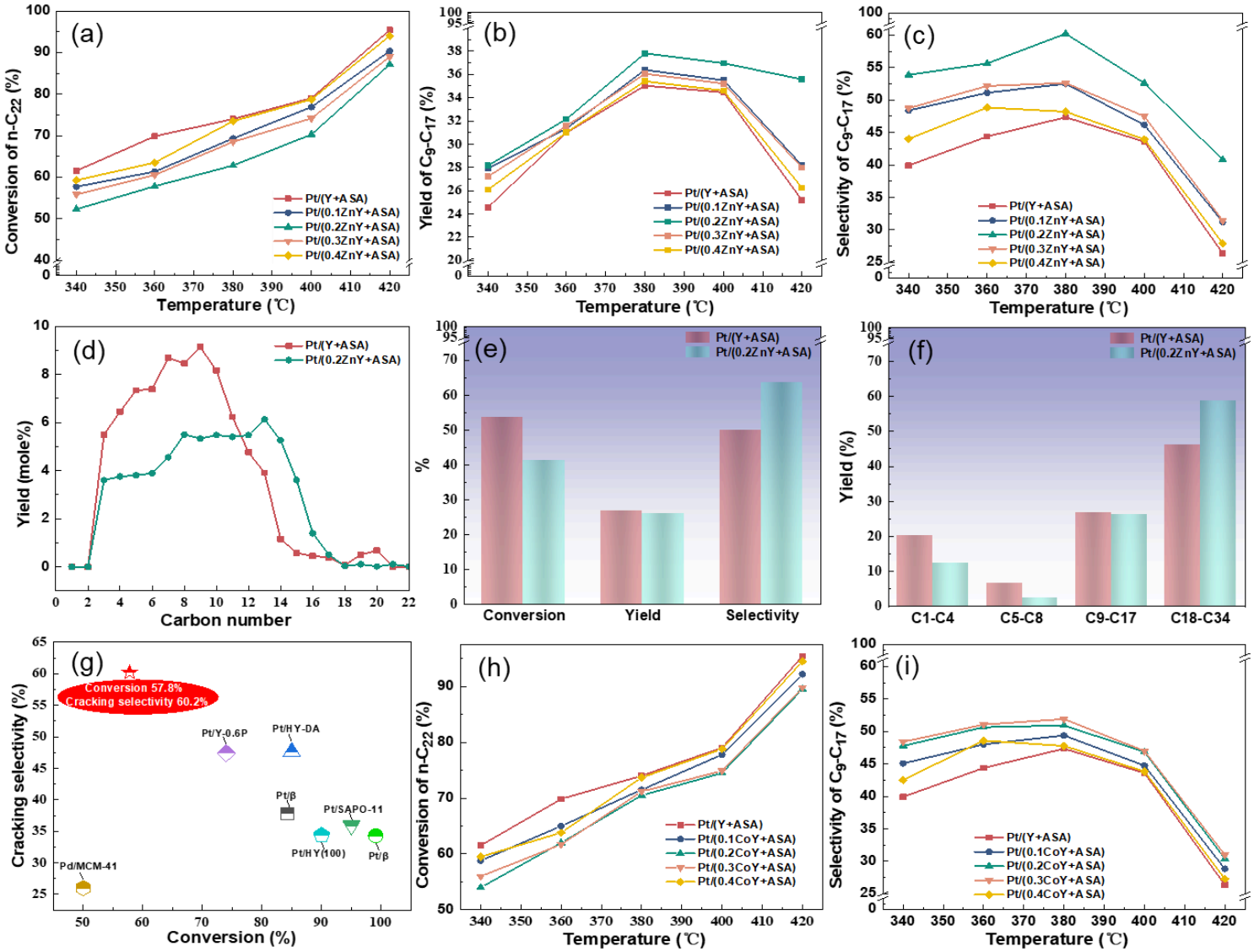


Figure 2

(a) n-C_{22} conversion, (b) C_9-C_{17} yield, (c) C_9-C_{17} selectivity over various catalysts under varying reaction temperatures, (d) molar carbon distribution of cracked products over Pt/(Y+ASA) and Pt/(0.2ZnY+ASA) catalysts at 380 °C, (e) FTW conversion, C_9-C_{17} yield and selectivity over Pt/(Y+ASA), Pt/(0.2ZnY+ASA) catalysts at 380 °C, (f) Products distribution fuel-range hydrocarbons: light gases (C_1-C_4), gasoline (C_5-C_8), and jet fuel (C_9-C_{17}) over Pt/(Y+ASA), Pt/(0.2ZnY+ASA) catalysts at 380 °C, (g) Comparison of hydrocracking performance with representative literature catalysts, (h) n-C_{22} conversion, (i) C_9-C_{17} selectivity over various catalysts under varying reaction temperatures.

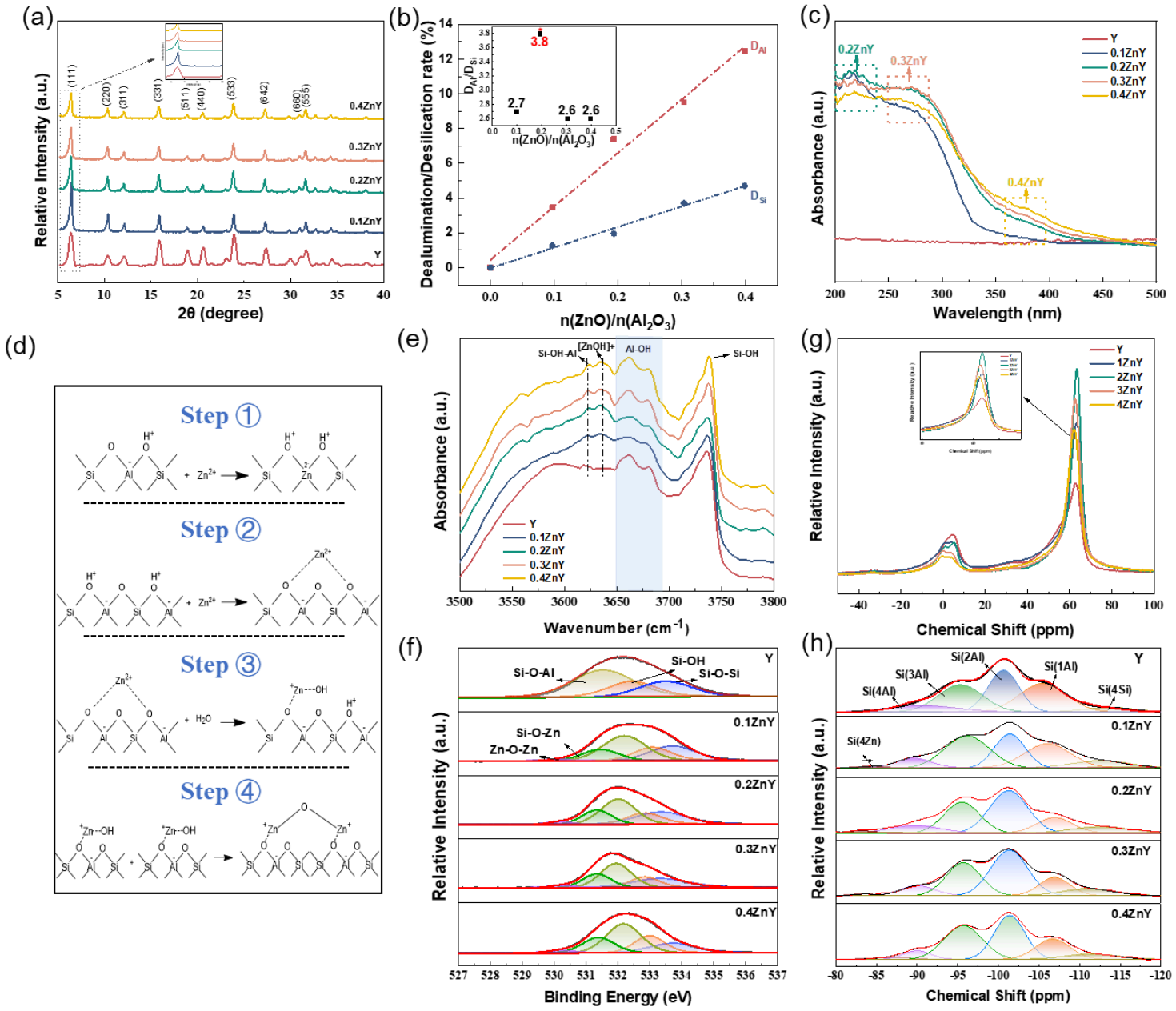


Figure 3

(a) XRD patterns of Y and xZnY zeolites. (b) Selective dealumination/desilication behavior of Zn-modified Y zeolites, (c) UV-Vis diffuse reflectance spectra of Y and xZnY zeolites, (d) Distinctive Chemical Reaction of Zn^{2+} with Y Zeolite, (e) OH-FTIR spectra in the hydroxyl region of Y and xZnY zeolites, (f) Deconvolutions of O 1s XPS spectra of Y and xZnY zeolites, (g) ^{27}Al MAS NMR spectra of Y and xZnY zeolites, (h) ^{29}Si MAS NMR spectra of Y and xZnY zeolites.

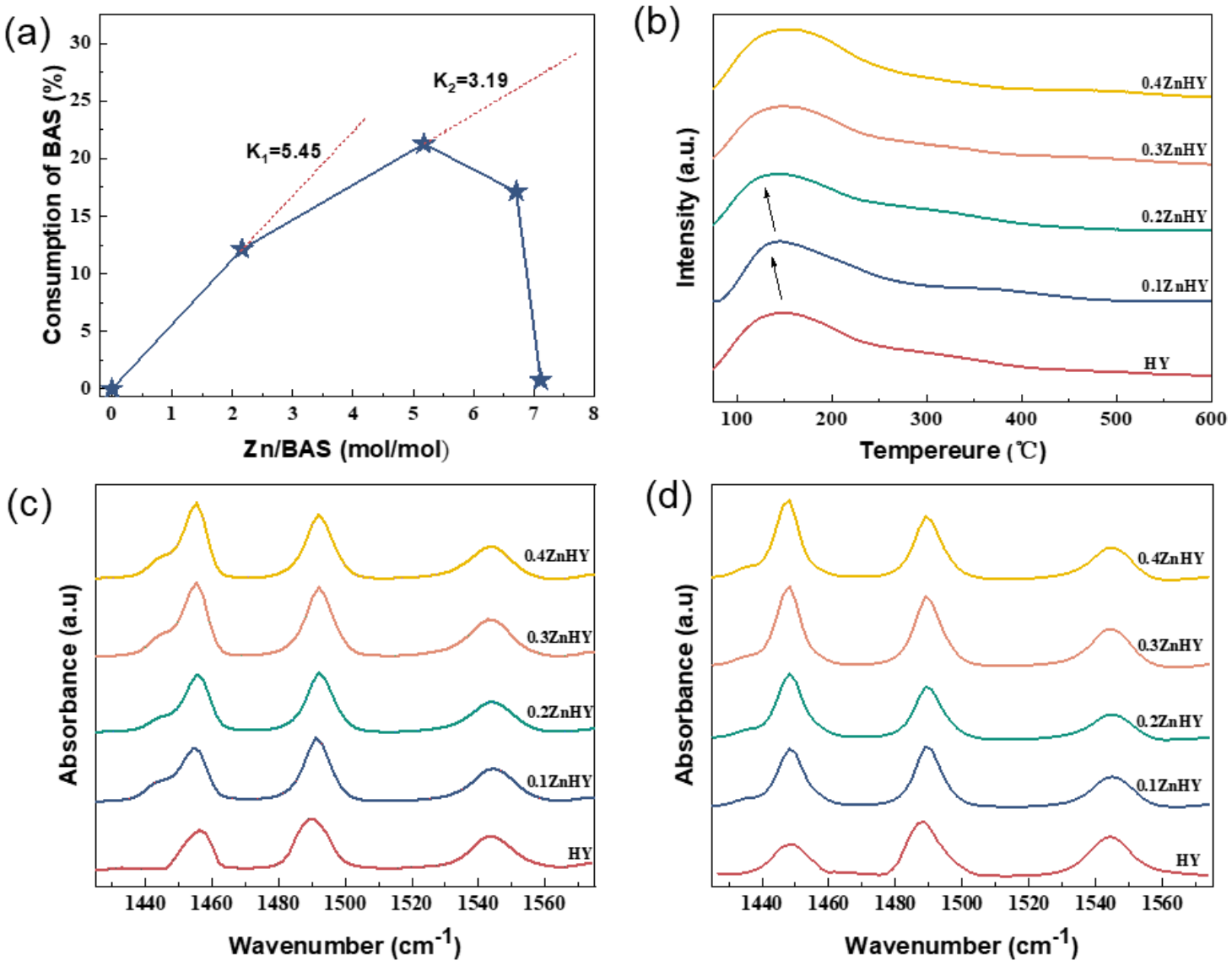


Figure 4

(a) Consumption of BAS of Zn/BAS ratios on Y and xZnY zeolites samples, (b) NH_3-TPD spectra of various Y zeolites, (c) Py-IR spectra of various Y zeolites after degassing at 200 ℃, (d) Py-IR spectra of various Y zeolites after degassing at 350 ℃.

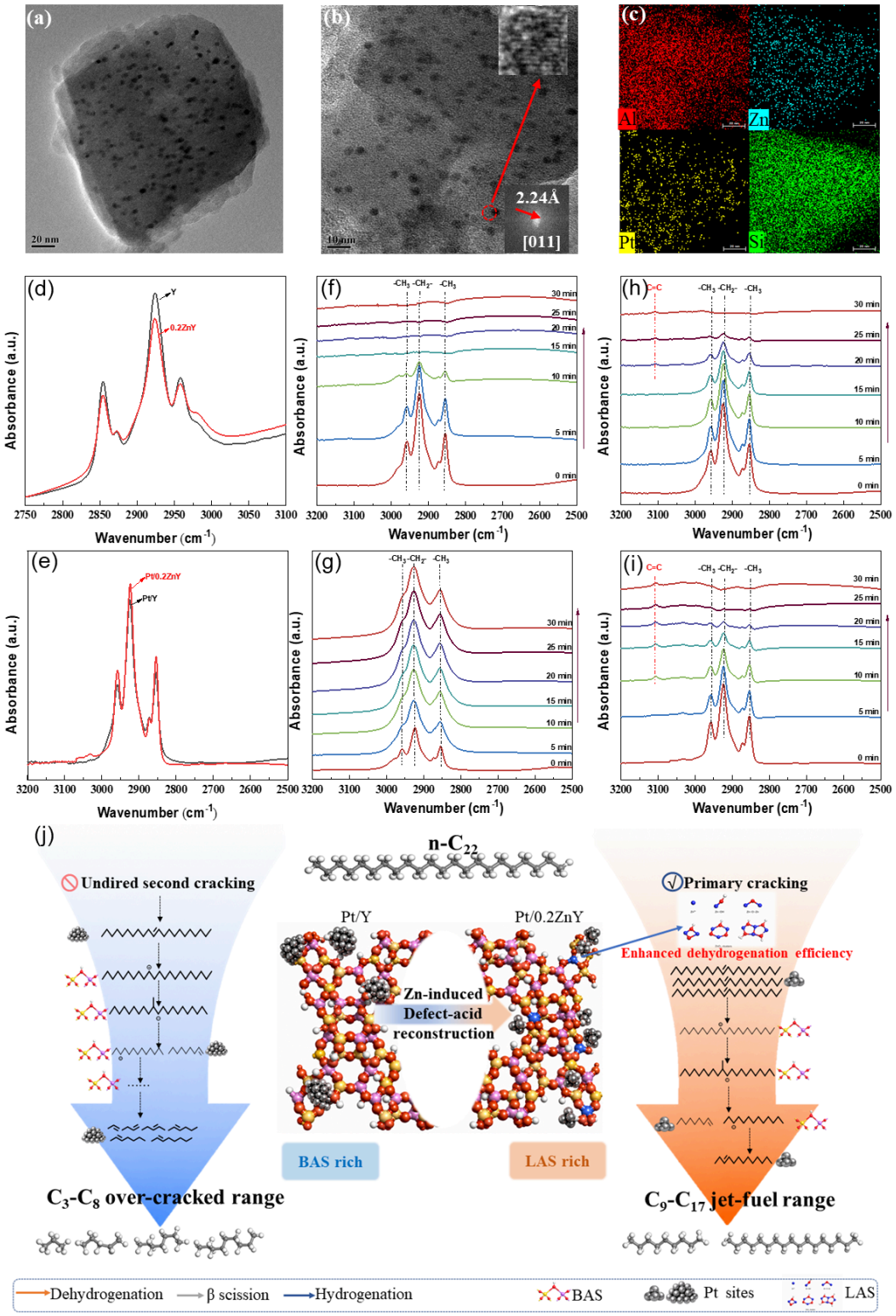


Figure 5

(a) TEM of Pt/(Y+ASA), (b) TEM of Pt/(0.2ZnY+ASA), (c) STEM of Pt/(0.2ZnY +ASA), Adsorption capacity of n-dodecane at 30 °C for 30 min on (d) Y and 0.2ZnY zeolites, (e) Pt/Y and Pt/0.2ZnY catalysts; In situ DRIFTS investigation of n-dodecane activation at 260 °C under Ar on (f) Y zeolite, (g) 0.2ZnY zeolite, (h) Pt/Y catalyst, (i) Pt/0.2ZnY catalyst, (j) Schematic diagram of Pt/ZnY catalyst for hydrocracking reaction process.

Supplementary Files

This is a list of supplementary files associated with this preprint. Click to download.

- 260609supportinginformation.docx
- 260509MLdataSI.xlsx